Electro-optic techniques in electron beam diagnostics

J. van Tilborg*, Cs. Tóth, N. H. Matlis, G. R. Plateau, and W. P. Leemans
Lawrence Berkeley National Laboratory, Berkeley, California

Abstract

Electron accelerators such as laser wakefield accelerators, linear accelerators driving free electron lasers, or femto-sliced synchrotrons, are capable of producing femtosecond-long electron bunches. Single-shot characterization of the temporal charge profile is crucial for operation, optimization, and application of such accelerators. A variety of electro-optic sampling (EOS) techniques exists for the temporal analysis. In EOS, the field profile from the electron bunch (or the field profile from its coherent radiation) will be transferred onto a laser pulse co-propagating through an electro-optic crystal. This paper will address the most common EOS schemes and will list their advantages and limitations. Strong points that all techniques share are the ultra-short time resolution (tens of femtoseconds) and the single-shot capabilities. Besides introducing the theory behind EOS, data from various research groups is presented for each technique.

INTRODUCTION

Electron accelerators are playing a major role in today's scientific landscape. Compact relativistic electron bunches, containing $> 10^9$ electrons, with a transverse size of several microns and a temporal duration of 10's to 100's of femtoseconds, can be utilized for numerous applications. On one hand one can think of experiments where the electrons are utilized directly (for example: colliders, electron diffraction, and magnetic switching). On the other hand, these compact bunches can produce intense electromagnetic radiation such as X-rays, gamma rays, ultraviolet photons, and terahertz (THz) radiation, among others (think for example of synchrotron radiation or free electron lasers). For all these applications, the quality of the electron bunch is a critical parameter. One way to assign a parameter for bunch quality is through the introduction of a beam brightness, defined as

$$\text{Brightness} = \frac{\text{Charge} \cdot \text{E}_{\text{kin}}}{\text{Duration} \cdot (\Delta\text{E}_{\text{kin}}/\text{E}_{\text{kin}}) \cdot \text{Emittance}}, \quad (1)$$

where E_{kin} is the electron kinetic energy with spread $\Delta\text{E}_{\text{kin}}$, and where the emittance represents the transverse emittance.

Each of the parameters listed in Eq. (1) needs to be measured and controlled for optimized accelerator performance. The work presented in this paper will address characterization of the temporal bunch duration, with the emphasis on bunches of ultra-short (femtosecond) duration.

* JvanTilborg@lbl.gov

Coherent radiation from electron bunches

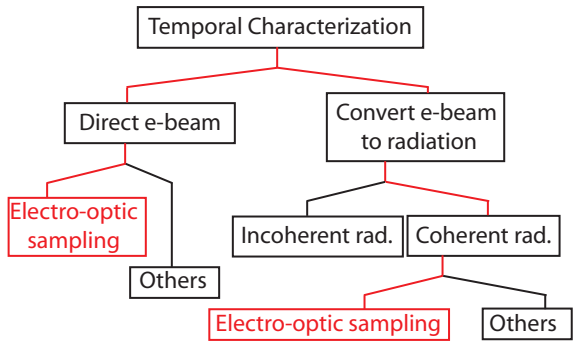

Figure 1: The technique of electro-optic sampling (EOS) can be applied to either the direct electron beam, or on the coherent radiation emission (typically at THz frequencies) that is produced by the electron bunch.

The temporal charge profile of an electron bunch can be labeled as $Q(t)$. The Fourier transformation of this profile is given by $Q(\omega) = \int dt Q(t) \exp(-\imath\omega t)$, where $\omega = 2\pi\nu$, with ν the frequency and ω the angular frequency. The spectral profile $Q(\omega)$ is complex (real and imaginary parts) and can be expressed as

$$Q(\omega) = |Q(\omega)|e^{\imath\phi(\omega)}, \quad (2)$$

where $|Q(\omega)|$ is the absolute spectrum and $\phi(\omega)$ the spectral phase. Note that only through measurement of both $|Q(\omega)|$ and $\phi(\omega)$ can the temporal profile $Q(t)$ be fully reconstructed.

As illustrated in Fig. 1, there are two paths to characterize the temporal duration of an electron bunch. The first path focuses on measurement of the field profile of the bunch itself (labeled as "Direct e-beam"), while the other path focuses on the emission of electro-magnetic radiation by the electron bunch. The mechanism for radiation emission can be transition radiation, diffraction radiation, Cherenkov radiation, Smith-Purcell radiation, or synchrotron radiation, among others. Since properties of the electron bunch duration are present in the emitted electromagnetic pulse, analysis of the radiation can lead to temporal bunch characterization.

The radiation can be categorized, see Fig. 1, as incoherent radiation (at wavelengths shorter than the bunch length) and coherent radiation (at wavelengths longer than the bunch length). It was demonstrated by Catravas *et al.* [1, 2] that through fluctuation interferometry of the incoherent radiation one can estimate the pulse duration. Also, a (sub)picosecond streak camera can be used to detect the pulse duration of the incoherent light [3]. Most

other radiation-based techniques focus on the coherent part of the spectrum, which is typically intense since it scales with the square of the number of electrons (while the incoherent part only scales linearly with the number of electrons). It has been shown that the field $E_{\rm coh}(\omega)$ of the coherent component of the spectrum can be described as

$$E_{\rm coh}(\omega) \propto Q(\omega)D(\omega), \qquad (3)$$

where $D(\omega)$ describes the effects of diffraction. The function $D(\omega)$ approaches $D = 0$ for long wavelengths and approaches $D = 1$ for short wavelengths. For example, for transition radiation, the function $D(\omega)$ was described by Schroeder *et al.* [4]. In Fig. 2 a coherent transition radiation pulse in the frequency domain (left) and in the time domain (right) is plotted for an electron bunch of duration τ_e =50 fs [root mean square (rms)], based on the definition $Q(t) = \exp\left[-t^2/(2\tau_e^2)\right]$. The diffraction [4] was based on a 500-μm transverse boundary size of the emission emitter. Note that the electric field profile of the coherent radiation pulse is almost identical to the field profile of the charge profile in both the time and frequency domain, except for the effects of diffraction. Diffraction will attenuate the spectrum at lower frequencies (see left plot in Fig. 2), while in the time domain a long negative field wing is introduced (see right plot). Through diffraction the condition $\int dt E_{\rm coh}(t) = 0$ is met, which is a condition required for any type of electro-magnetic radiation.

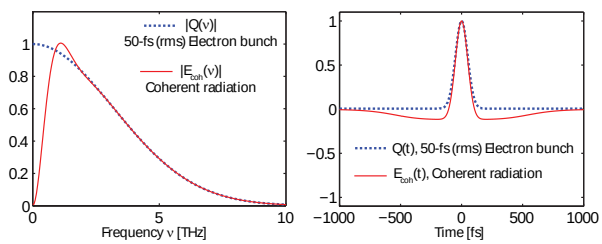

Figure 2: Example of a coherent radiation pulse (red solid curve) emitted from a 50-fs (rms) electron bunch. The left plot shows the similarity in the frequency domain (the difference is the attenuation due to diffraction at low frequencies), while the right plot shows the similarity in the time domain (the difference is the appearance of long-timescale negative field wings).

The spectrum on the left side of Fig. 2 also illustrates that both the charge profile and the coherent radiation pulse for a femtosecond electron bunch have spectral components in the terahertz (THz) regime. Therefore, both the electric field profile of the electron bunch and the coherent radiation pulse will share the same label "THz pulse" in the next sections of this paper, with field profile $E_{\rm THz}(t)$.

Several techniques exist for analyzing the absolute spectrum of the coherent radiation (and missing the spectral phase), such as spectral measurements with a far-infrared spectrometer (also referred to polychromator) [3, 5] or a Michelson or Martin-Puplett interferometer [3, 6, 7]. A more recently developed diagnostic technique is electro-optic sampling (EOS) [8, 9], which is a laser-based technique. This technique offers unique advantages, which include

- Temporal resolution on the order of 10's of femtoseconds
- Non-destructive to the electron beam
- Room-temperature operation (no bolometers)
- Single-shot capabilities
- Measures relative timing to other pump/probe beams
- Yields exact charge profile $Q(t)$, and not just $|Q(\omega)|$

As mentioned earlier, see Fig. 1, the temporal profile of an electron bunch can also be obtained through techniques measuring directly the field profile of the bunch. Examples are the radio frequency (RF) zero-phasing method [10, 11] (also referred to as the RF streak method), or laser-electron interaction experiments such as laser-induced electron deflection [12]. In addition to being applied to coherent radiation, EOS can also be applied directly to the electric field of the electron beam, as shown in the diagram in Fig. 1. Again, the same set of advantages for EOS as itemized earlier are valid. Note that EOS on the electron beam directly has to occur *in situ* (in the vacuum chamber), while coherent radiation could easily be transported out of the vacuum chamber to any location of choice, making it easier to access the EOS setup. Of course, by setting up a radiation beam path, issues such as clipping, aberrations, dispersion in transmissive optics, and spectral-dependent reflectivity have to be considered and could potentially effect the analysis [13].

BASICS OF ELECTRO-OPTIC SAMPLING

In electro-optic sampling [8, 9], the THz pulse (as mentioned before, this could refer to the electron bunch or the coherent radiation pulse since both have frequency components in the THz domain) induces a change in index of refraction in an electro-optic crystal. This change can be measured by a near-infrared (NIR) laser pulse $E_L(t)$. The electro-optic effect is a second-order nonlinear or $\chi^{(2)}$ effect. The EO crystal, having no or little birefringence in absence of THz fields, will become birefringent upon presence of a THz pulse. The birefringence can best be described by the index ellipsoid. This effect is sketched in Fig. 3. In this paper, the family of EO crystals of cut <110> is considered, for which the crystal axis (z' axis) lies in the plane of the cut. The relations between the crystal's z' axis, the THz field polarization vector, and the major and minor axes of the induced index ellipse are well described by Chen *et al.* [14].

Since the THz pulse field strength is time-dependent [$E_{\rm THz}(t)$], the change in index ellipse will also follow the THz pulse temporal profile. The change in index ellipsoid will leave an imprint on the accumulated phase of the laser pulse. The polarization of the laser pulse can be expressed in the coordinate system of the index

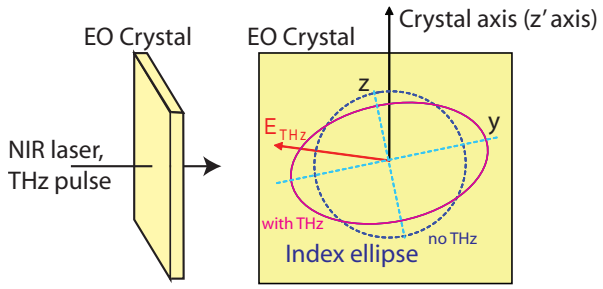

Figure 3: Overview of the field and crystal vectors involved in EOS. For <110> cut EO crystals, the crystal axis (or z' axis) lies in the crystal cut (crystal plane). Depending on the THz pulse field strength, the index ellipsoid for a NIR laser changes from circular (no birefringence) to elliptical, with major and minor axes z and y, respectively. The rotation orientation of the index ellipse is a function of the THz field vector with respect to the crystal z' axis.

ellipse y and z, see Fig. 3. We therefore can define $E_L(t) = E_{L,0}\exp(-\imath\omega_0 t)\exp[-t^2/(2\tau_L^2)]$, with τ_L the laser pulse duration (rms), and $E_{L,0} = E_y\exp(\imath\phi_{0,y})\ \vec{e_y} + E_z\exp(\imath\phi_{0,z})\ \vec{e_z}$. The polarization phase components $\phi_{0,y}$ and $\phi_{0,z}$ reflect the polarization state (linear, elliptical, or circular) and are constants determined by the optical elements in the laser's optical path such as quarter- and half-wave plates.

During propagation through the EO crystal, the change in index of refraction δn_z along the ellipsoid axes z, as well as δn_y along the ellipsoid axes y, is [14]

$$\begin{aligned}\delta n_z &= \frac{n_0^3 r_{41} E_{\mathrm{THz}}}{4}\left(cos\phi + \sqrt{1+3\sin^2\phi}\right)\\ \delta n_y &= \frac{n_0^3 r_{41} E_{\mathrm{THz}}}{4}\left(cos\phi - \sqrt{1+3\sin^2\phi}\right)\end{aligned} \quad (4)$$

with ϕ the angle between the crystal z' axis and the THz polarization. In this paper we will consider $\phi = \pi/2$, in which case the axes z and y are at 45 degrees with respect to the crystal z' axis [14]. Also, r_{41} is the electro-optic coefficient of the EO crystal and n_0 is the index of refraction at the central wavelength of the NIR pulse. The EO-induced phase shift for the laser's polarization component along axis j of the ellipse is given by $\delta\phi_j = \delta n_j L 2\pi/\lambda_0$, with $\lambda_0 = 800$ nm and L the EO crystal thickness.

Since E_{THz} in Eq. 4 has a temporal dependency one might at first sight expect the phase shift along the ellipse axis to be simply $\delta\phi_j(t) \propto E_{\mathrm{THz}}(t)$. However, several crystal effects can not be overlooked. Think of 1) absorption of some THz frequencies, 2) dispersion of the THz pulse, and 3) a velocity mismatch between the laser's group velocity and the individual THz phase velocities. These effects can best be described by a crystal transfer function $T_{\mathrm{crystal}}(\omega)$. The actual phase shift along axis j is defined as $\Gamma_j(t)$. In order to relate $\Gamma_j(t)$ to $E_{\mathrm{THz}}(t)$ and T_{crystal}, it is easiest to operate in the frequency domain, in which case [8, 15]

$$\Gamma_j(\omega) = \frac{2\pi}{\lambda_0} L\delta n_j(\omega) T_{\mathrm{crystal}}(\omega), \quad (5)$$

with δn_j defined by Eq. (4). It was shown [15] that $T_{\mathrm{crystal}}(\omega)$ is mainly dependent on the real and imaginary index of refraction of the EO crystal in the THz regime, and is given by

$$T_{\mathrm{crystal}}(\omega) = \frac{2}{1+n_{\mathrm{THz}}}\cdot\frac{\exp[\imath L(n_{\mathrm{gr}}-n_{\mathrm{THz}})\frac{\omega}{c}]-1}{\imath\frac{\omega}{c}(n_{\mathrm{gr}}-n_{\mathrm{THz}})}, \quad (6)$$

with n_{gr} the group velocity of the laser and $n_{\mathrm{THz}} = n_{\mathrm{THz}}(\omega)$ the complex index of refraction.

To summarize the previous discussion, let's label the modulated laser field as $E_M(t)$. The field projections of $E_M(t)$ along the y and z axis are $E_{M,y}(t)$ and $E_{M,y}(t)$. The field projection $E_{M,j}(t)$ is given by

$$E_{M,j}(t) = E_{L,j}(t)e^{\imath\Gamma_j(t)} \quad (7)$$

Note that a more detailed theoretical description has been written by Jamison *et al.* [9]. Here the modulated field profile was found to be $E_{M,j}(t) = E_{L,j}(t) + \frac{d}{dt}[E_{L,j}(t)\cdot\Gamma_j(t)]$. For THz frequencies much smaller than $\omega_0 = 2\pi c/\lambda_0$, and for THz-induced EO phase retardations less than 1 rad, this expression reduces to Eq. (7). It is therefore important to note that the expressions used in this paper are following those two assumptions.

There are a large variety of experimental configurations possible that detect the added phase term $\Gamma_j(t)$. The laser can have arbitrary polarization (linear, elliptical, or circular), its polarization vector can be at any arbitrary angle with respect to the index ellipse, and/or a polarizer can be added after the EO crystal. The next two sections will be devoted to various techniques that allow the user to measure $\Gamma_j(t)$, leading to $E_{\mathrm{THz}}(t)$ and $Q(t)$. In both sections, the phase dependent time $\Gamma_j(t)$ will be converted to an intensity modulation on the laser envelope. The first section will focus on techniques where the intensity-modulated laser beam is analyzed in the time domain, while the second section will focus on analyzing the modulated laser pulse in the frequency domain through measurement of the spectrum of the laser pulse.

ELECTRO-OPTIC SAMPLING IN THE TIME DOMAIN

The EOS schemes described in the remaining sections are based on the laser propagating through an EO crystal, oriented such that the major laser polarization axis, as indicated in Fig. 4, is at 45 degrees with respect to the ellipsoid axes. In Fig. 4 the laser polarization state is linear or elliptical, but with conservation of generality the case of circular polarization can be considered as well. The only difference between the various polarization states is the ratio of the field amplitudes E_y and E_z, as well as the difference in phase $|\phi_{0,y} - \phi_{0,z}|$. As indicated in Fig. 4 the polarizer, positioned after the EO crystal, is only transmitting the laser

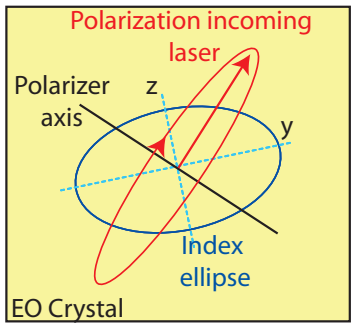

Figure 4: In most EOS schemes the THz-induced laser phase modulation is converted to a laser amplitude modulation. Typically, the laser's major polarization axis is at 45 degrees with respect to the index ellipsoid axes y and z. After propagation through the EO crystal, the laser beam passes through a polarizer (also referred to as analyzer), which only transmits the polarization component perpendicular to the incident laser's major polarization axis.

fields with a polarization component at 90 degrees with respect to the polarization vector of the laser. It was shown by Eq. (4), and using the geometry $\phi = \pi/2$, that the difference in index of refraction $\Delta n(t)$ is given by $\Delta n(t) = \delta n_z - \delta n_y = n_0^3 r_{41} E_{\rm THz}(t)$. This leads to a net phase shift following Eq. (5) of $\Gamma(\omega) = (2\pi/\lambda_0) L \Delta n(\omega) T_{\rm crystal}(\omega)$. A simple construction of Jones matrices [16] describes the evolution of the electric field vector (amplitude and phase) through any optical system, such as polarizers, wave plates, phase shifts induced in the EO crystal, etc. The Jones matrices allow for calculation of the electric field $E_M(t)$, and intensity $I_M(t) = |E_M(t)|^2$, of the laser passing through the polarizer. For example, for circular polarizer laser light, defined as $E_y = E_z$ and $|\phi_{0,y} - \phi_{0,z}| = \pi/2$, it can be shown that

$$I_M(t) = I_L(t) \cdot \frac{1}{2} \left[1 + \sin \Gamma(t)\right]. \tag{8}$$

For linear polarized light, for which $E_y = E_z$ and $\phi_{0,y} = \phi_{0,z}$, the transmitted laser intensity (or energy) is now

$$I_M(t) = I_L(t) \cdot \sin^2 \left[\Gamma(t)/2\right]. \tag{9}$$

Note that the sign information in this linear case is lost, although the sensitivity (change in transmitted intensity for a small THz field) has increased. In the next paragraphs, various experimental techniques to measure $I_M(t)$ [and therefore $\Gamma(t)$] will be considered. For simplicity we will assume a circular polarization state of the incoming laser pulse.

Scanning technique

In the first and simplest technique, the laser pulse length τ_L is short compared to the THz pulse length. Typically, laser pulse lengths of few tens of fs can easily be delivered to the EO crystal. A photo-diode can measure the time-integrated laser energy $I_{\rm diode} \propto \int dt I_M(t)$ that has passed through the polarizer. The diode signal (measuring energy I) versus time delay between laser and THz pulse, following Eq. (8), is then given by

$$\begin{aligned} I_{\rm diode}(\tau) &= \int dt I_L(t-\tau) \cdot \frac{1}{2} \left[1 + \sin \Gamma(t)\right] \\ &\simeq \frac{1}{2} \left[1 + \sin \Gamma(\tau)\right], \end{aligned} \tag{10}$$

where the second step is only valid for sufficiently short laser pulse lengths. In reality, the effect of the non-zero laser pulse length will come into play through the Fourier transformation of the envelope of the laser pulse intensity, or $I_{\rm env}(\omega) = \int dt \exp\left(-t^2/\tau_L^2\right) \exp\left(-\imath\omega t\right)$. In first approximation, the retrieved EO profile $\Gamma(\omega)$ is in fact $\Gamma(\omega) I_{\rm env}(\omega)$. The measurement of $\Gamma(\tau)$ needs therefore to be corrected for the laser pulse envelope. For example, a laser pulse with a rms (field) pulse duration of $\tau_L = 30$ fs, and thus an intensity full-width-at-half-max of $2\tau_L\sqrt{\ln 2} = 50$ fs, will result in a spectral cut-off [half-max of $I_{\rm env}(\nu)$] in the THz domain around $\nu = 9$ THz.

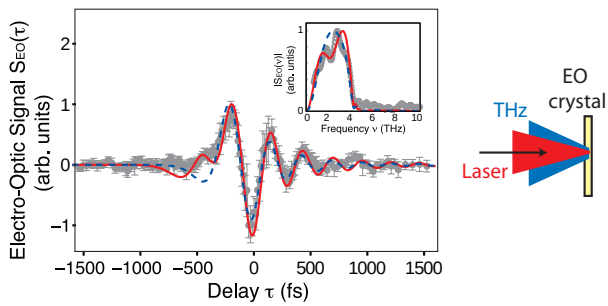

Figure 5: Example of a scanning EOS measurement of coherent radiation [$S_{\rm EO}(\tau) = I_{\rm diode}(\tau)$]. The radiation, together with the laser pulse, was focused on a ZnTe crystal. The data was published by van Tilborg *et al.* [17]. It was based on THz radiation from a laser wakefield accelerator. The inset shows the Fourier transformation of the data. The red curve is a fit based on a Gaussian electron bunch of length 50 fs (rms).

An example of a scanning measurement is presented in Fig. 5, published by van Tilborg *et al.* [17]. The data was taken on coherent transition radiation from a laser wakefield accelerator. The laser and THz beams were focused onto the EO crystal, such that the THz field strength was optimized and spatial overlap of the laser and THz profile was guaranteed. The Fourier transformation of the data is plotted in the inset. The data is also fitted with a modeled EO-modulated profile from a 50 fs (rms) electron bunch. Note that the sharp cutoff in the data at 4 THz is due to the crystal transfer function of 200-μm-thick ZnTe crystal. Note that the form factor $Q(\nu)$ a 50 fs (rms) electron bunch has a spectral half max at $\nu = 3.7$ THz, which falls just within the bandwidth of the ZnTe crystal. This limits the use of ZnTe crystal to bunches longer than ~50 fs (rms).

Because of the scanning nature of this technique, its success relies intrinsically on the stability of the electron accelerator and THz emission properties. Note that the use of elliptical or circular polarized laser light, see Eq. (8), yields sign-resolved THz field information. In the case of probing directly the fields of the electron bunch, this is not relevant and linear polarized laser pulses can be applied, which is more favorable since the polarizer throughput scales more dramatically with THz field strength in this configuration.

Since most accelerators do not possess excellent shot-to-shot reproducibility, either in the electron bunch properties or in the arrival time with respect to the laser, single-shot EOS techniques are strongly favorable. The next few section will introduce several single-shot detection schemes.

Spatio-temporal mixing or echelon-based technique

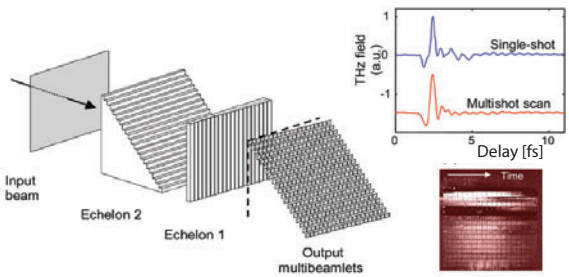

Figure 6: Overview of the experimental results from Kim *et al.* [18], in which two echelons (see left illustration) where used to create a series of beamlets out of the laser beam. Since each beamlet overlaps at the THz focus with a different time delay , the THz temporal profile (see figure top right) is imprinted in the spatial laser profile in the far field (see figure bottom right).

A simple extension of the previous technique is a technique demonstrated by Kim *et al.* [18]. Just as in the scanning geometry, a short laser pulse is used. However, through a combination of two echelons, see left part of Fig. 6, an array of beamlets is created out of the laser laser beam, each with a specific delay time. This is a direct consequence of the fact that each beamlet propagated through a different thickness of material in the echelons. Once this collection of beamlets is focused onto the EO crystal, each beamlet is overlapped with the THz pulse, but at a different relative temporal delay. In the far field, after propagating through a polarizer, the beamlets spread out again spatially and can be imaged by a camera, see the bottom right image in Fig. 6. By plotting the modulated measured energy of each beamlet a full THz profile can be reconstructed, see the top right part of Fig. 6. The retrieved waveform is compared to a waveform obtained with a standard scanning technique.

This technique is labeled as "spatio-temporal mixing technique" because the beamlets, which split up the larger laser beam into little spatial domains, represent different temporal delays at focus. The technique has not been applied yet to direct electron bunches or THz pulses produced by electron bunches, but was demonstrated [18] on a laser-based THz source. The same comments for the temporal resolution as for the scanning technique are valid, namely a resolution limited by the laser pulse length. Note that for ultra-short laser pulses (<30 fs), the beamlet-dependent dispersion through the echelons has to be accounted for and might limit its application.

Non-collinear cross-correlation between THz and laser pulses

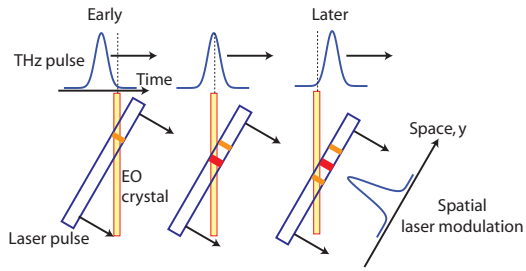

Figure 7: Illustration explaining the basic concept of non-collinear cross-correlation, in which the propagation vectors of the THz pulse and laser pulse are tilted with respect to one other. At early times (see left image), only a fraction of the transverse profile of the laser pulse is overlapped in the EO crystal with the front of the THz pulse. At later times (see right images), the overlap is occurring for a different spatial part of the laser beam, and the overlap also occurs at a different time slice of the THz pulse. Therefore, the temporal THz profile is imprinted on the spatial transverse intensity profile of the laser, which is an easy feature to measure with a camera.

Another single-shot technique that measures the THz modulation in the time domain is intrinsically based on non-collinear propagation of the THz pulse and the laser pulse onto the EO crystal, see Fig. 7. It is important that neither the laser beam nor the THz pulse are focused, but remain collimated. In fact, we have to assume that both beams have no spatial-dependent field features. At a specific moment in time, see for example the left plot in Fig. 7, the THz field in the EO crystal overlaps with only a spatial fraction of the laser pulse. There is direct correlation with the transverse spatial position within the laser beam and the relative time delay between both pulses. For example, subsequent plots in Fig. 7 show that different transverse spatial regions in the laser beam correspond to different relative delays. Therefore, by measuring (after propagating through a polarizer) the transverse energy distribution of the laser profile, a complete temporal THz profile can be reconstructed.

This technique was demonstrated on a laser-based THz source by Shan et al. [19], and demonstrated on the THz fields (direct electron beam) from an electron accelerator

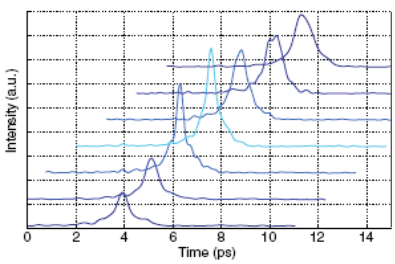

Figure 8: THz profiles obtained through the non-collinear cross-correlation technique, measured by Cavalieri *et al.* [20]. The electric fields of the electron bunch were measured directly by propagating the electron bunch close to the EO crystal. Each profile in the figure corresponds to a different accelerator tuning setting.

by Cavalieri et al. [20], as shown in Fig. 8. The electron bunches that they characterized were found to have a minimum pulse length of 270 fs. Another advantage of this technique is the relative large single-shot temporal window. For each shot, one not only gets the charge profile, but also the relative timing with respect to the laser pulse. Just as in the previous two subsections, time resolution is limited only by the laser pulse length. Disadvantages of this technique could be the reliance on a uniform transverse THz and laser profile. Also, the EO effect could be weak due to the lack of focusing. However, in case of measurement on the electron beam directly this last point is less critical since the electron bunch is typically dense with large transverse fields.

Non-collinear cross-correlation between laser and THz-modulated-laser pulses

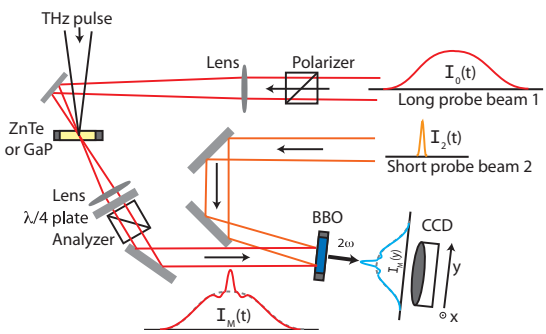

Figure 9: Overview of the setup for single-shot detection based on the non-collinear cross-correlation of a short laser beam (probe beam 2) and a long THz-modulated laser beam (probe beam 1). Through frequency doubling in the BBO crystal, the THz imprint on the envelope of probe beam 1 can be recorded by a camera in a single-shot.

Another non-collinear cross-correlation scheme was proposed by Jamison *at al.* [21] and demonstrated on electron accelerators by Berden *et al.* [11, 22] and van Tilborg *et al.* [13]. This technique is closely related to the previous cross-correlation technique, but there are a few critical differences. First of all, the laser beam incident on the EO crystal is now much longer than the THz pulse, see $I_0(t)$ in Fig. 9. This can be achieved by either suppressing the bandwidth of an ultra-short laser, or by chirping the laser. The laser and the THz radiation are both focused on the EO crystal for maximum EO effect. After propagating through the polarizer, see Fig. 9, the THz-modulated-laser beam has a time-dependent intensity modulation $I_M(t)$ as defined by Eq. (8). In second stage, the intensity-modulated long laser pulse can be measured in a single-shot with a second laser probe beam $I_2(t)$, which is now short (tens of femtoseconds), based on the same non-collinear cross-correlation geometry as discussed in the previous section. The second probe beam will define the temporal resolution of this technique. Through non-collinear frequency doubling in a BBO crystal, the spatial profile of the frequency-doubled beam $I_{2\omega}(y)$, as measured by a CCD camera, contains the THz imprint on probe beam I_0, or

$$\begin{aligned} I_{2\omega}(y) &\approx I_M(\tau) \\ &= \int dt I_2(t-\tau)\cdot I_0(t)\frac{1}{2}\left[1+\sin\Gamma(t)\right] \\ &\simeq I_0(\tau)\frac{1}{2}\left[1+\sin\Gamma(\tau)\right], \end{aligned} \tag{11}$$

By measuring the blue profile, and dividing it by a reference profile when no THz radiation was present, the THz profile $\Gamma(t)$ can be retrieved.

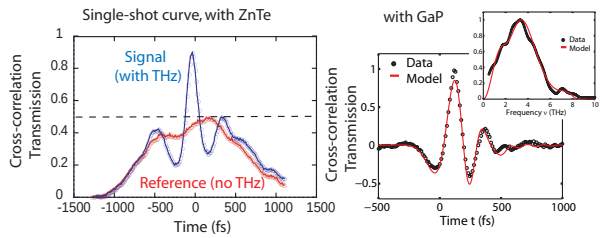

Figure 10: Data from van Tilborg *et al.* [13] using the non-collinear cross-correlation scheme between a short laser and a longer THz-modulated laser pulse. The left image shows a measurement on a ZnTe crystal, while the main figure on the right shows a GaP measurement. The Fourier transformation in the inset indicates the presence of THz radiation up to 7-8 THz. The red curve is a fit based on THz radiation from a 45 fs (rms) electron bunch.

Results from this technique, measured by van Tilborg *et al.* [13], are shown in Fig. 10. The data presented in Fig. 10 was obtained with the same accelerator of which scanning data was presented in Fig. 5. The left plot show a single-shot trace with a ZnTe crystal, while the right plots are based on EOS in a GaP crystal. The red curve for the right plots was based on modeled THz radiation from a 45 fs (rms) electron bunch. Note that the GaP crystal does not have a cut-off around $\nu = 4$ THz like ZnTe, but can resolve

the full THz spectrum up to $\nu = 8$ THz. The measured profile for $\Gamma(t)$ is in reality of convolution of the actual $\Gamma(t)$ with the laser pulse envelope of the second short laser probe $I_{\mathrm{env},2}$, and has to be taken into account. This technique seems to deliver all the necessary information in a single-shot. One can study shot-to-shot fluctuation in charge profile, or in timing jitter. Disadvantages of this technique are its complexity, resulting from a geometry based on 3 beams and 2 nonlinear crystals. Also, the power balance of the two laser beams is critical in order to obtain a clean frequency-doubled image but without damaging the EO crystal.

ELECTRO-OPTIC SAMPLING IN THE LASER'S FREQUENCY DOMAIN

Another set of techniques relies on measuring the spectrum of the THz-modulated chirped laser beam. Both the THz and laser beam are focused on the EO crystal. In these geometries an ultra-short laser is chirped to a pulse length much longer than the THz pulse. The expression for the electric field of the incident laser profile is given by

$$E_{L,j}(t) = \vec{e_j} \exp(\imath\phi_{0,j}) \exp\left[\frac{(1-\imath b/2)t^2}{2\tau_{\mathrm{FL}}^2(1+b^2/4)}\right] \exp[\imath\omega_0 t], \tag{12}$$

with b the chirp parameter and τ_{FL} the rms Fourier limited pulse duration. The actual rms pulse duration is $\tau_L = \tau_{\mathrm{FL}}\sqrt{(1+b^2/4)}$. Note that the instanteneous frequency $\omega_{\mathrm{inst}}(t)$ of the chirped laser pulse is given by

$$\omega_{\mathrm{inst}}(t) = \omega_0 + \frac{b}{2\tau_{\mathrm{FL}}^2(1+b^2/4)}t. \tag{13}$$

Just as mentioned earlier, after propagation through the EO crystal, an extra phase shift is introduced, leading to a modulated laser pulse $E_{M,j}(t) = E_{L,j}(t) \cdot \exp[\imath\Gamma_j(t)]$. Although the information on the THz profile could potentially be retrieved by measuring the power spectrum $|E_{M,j}(\lambda)|^2$ of the phase-modulated laser probe, the techniques described in this paper rely again on the conversion of the phase modulation to an amplitude modulation. Just as in last section, this can be done by using the polarization geometry of Fig. 4, and using a polarizer. This results in a time dependent intensity oscillation on the chirped laser pulse, as sketched on the right part of Fig. 11.

Spectral encoding for ps-type THz pulses

The simplest technique based on THz-pulse retrieval from the laser spectrum is only applicable for THz frequencies ν for which $\sqrt{\tau_{\mathrm{FL}}\tau_L} < 1/\nu$. For example, an electron bunch of length 400 fs (rms) contains THz frequencies up to 0.5 THz (spectral half-max at ν =0.46 THz). By using a laser pulse of τ_L =3.5 ps duration, from a Fourier limited pulse length of $\tau_{\mathrm{FL}} = 50$ fs, one can see that this requirement is met (indeed 418 fs $<$ 2 ps). This example is shown in Fig. 11. The THz pulse is plotted in the top left graph. The orange curve in the inset of the bottom left

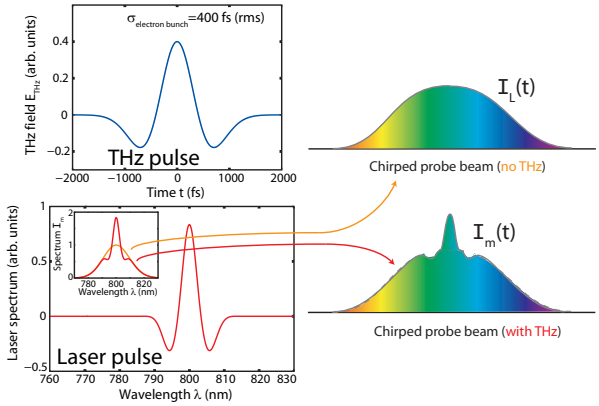

Figure 11: The right images show the intensity modulation of a THz pulse on the envelope of a chirped long laser pulse. The THz pulse itself is plotted on the top left plot, based on a electron bunch of 400 fs (rms) length. The spectrum of the modulated laser pulse $I_M(\lambda)$ is shown in the bottom left graph. Through a conversion of parameters $\lambda \rightarrow t^*$ (based on a linear chirp rate), it can be shown that the normalized spectral modulation is identical to the original THz pulse.

graph shows that laser spectrum without THz modulation, while the red curve is plotted with EO modulation considered. The normalized difference between both curves $[I_M(\lambda) - I_L(\lambda)]/I_L(\lambda)$ is also shown in the main figure on the bottom left.

It was shown by several groups [23, 24] that the modulated spectrum can be converted back to the time domain based on the conversion $\lambda \rightarrow t^*$, with $\lambda = 2\pi\omega_{\mathrm{inst}}/c$ based on Eq. (13). This conversion leads to the measurement of $I_M(\lambda) \rightarrow I_M(t^*)$. Since we know the relation of $I_M(t^*)$ to $\Gamma(t^*)$ through Eq. (8) we have reconstructed a complete sign-resolved THz profile. Indeed, the red curve in Fig. 11 is identical to the original THz profile after the conversion $\lambda \rightarrow t^*$ based on Eq. (13).

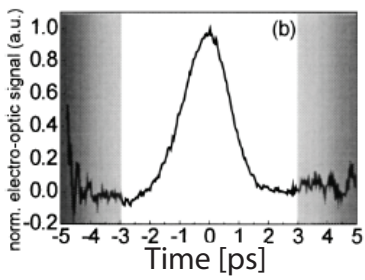

Figure 12: Data from Wilke *et al.* [25] based on the single-shot measurement of the spectrum of a THz-modulated laser pulse ($\tau_{\mathrm{FL}} = 30$ fs and $\tau_L = 4.5$ ps). The wavelength axis has been converted to a time axis based on Eq. (13). The electron bunch was found to have a length of 1.7 ps (FWHM).

An example of this technique is plotted in Fig. 12. The

data, published by Wilke *et al.* [25] was taken on the electric field of the electron bunch directly. The parameters for the laser were $\tau_{\rm FL} = 30$ fs, $\tau_L = 4.5$ ps, and the retrieved bunch length had a duration of 1.7 ps. The wavelength axis of the plot in Fig. 12 has already been converted to a time axis through the $\lambda \rightarrow t^*$ conversion based on Eq. (13).

Although the time resolution for the spectral encoding technique is limited to several hundreds of femtoseconds, this technique is otherwise quite advantageous. It relies on only one low-power laser pulse and only one nonlinear crystal (the EO crystal), and the alignment onto the spectrometer is fairly straightforward. The full THz field profile (amplitude and phase) is reconstructed in a single shot through a simple parameter conversion $\lambda \rightarrow t^*$. A calibration can be easily applied by adding a know temporal delay between the THz and laser pulse and observing the spectral shift.

Spectral encoding for fs-type THz pulses

Unfortunately, the previous analysis breaks down if THz frequencies are present in the THz pulse for which $\sqrt{\tau_{\rm FL}\tau_L} < 1/\nu$ is no longer valid. This is the case for electron bunches shorter than 500 fs. An example of the breakdown is shown in Fig. 13, where an electron bunch of 50 fs (rms) is plotted as the solid curve in the left plot. The top right image in the right plot again shows a sketch of the time-dependent intensity modulation, while the inset on the left of the same figure shows the modulated laser spectrum (red curve) versus the original laser spectrum (orange curve). The normalized difference between both curves $[I_M(\lambda) - I_L(\lambda)]/I_L(\lambda)$ is shown in the main plot of the right figure. As one can see, upon conversion of wavelength to time, the retrieved profile $I_M(t^*)$ does not resemble the original THz profile at all, mainly due to the presence of spectral oscillations.

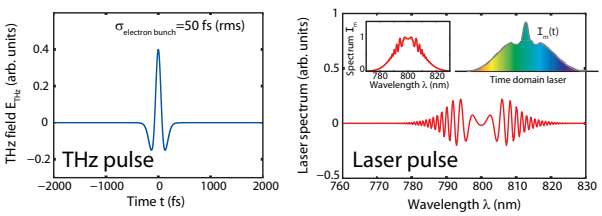

Figure 13: The left plots shows the THz profile of a 50 fs (rms) electron bunch. The spectrum $I_M(\lambda)$ of the THz-modulated laser pulse is plotted on the right. Due to the short bunch duration, the spectrum shows heavy modulation. Upon conversion of $\lambda \rightarrow t^*$, the retrieved profile $I_M(t)$ does not resemble the original THz profile.

It was shown theoretically by Yellampalle et al. [26], and demonstrated experimentally on laser-produced THz pulses by Kim et al. [27], that an algorithm can by applied on the heavy modulated spectral interferogram in order to retrieve the original THz pulse. The algorithm is based on detailed knowledge of the chirped laser beam (chirp parameter, Fourier-limited pulse length, and pulse shape). It has to be pointed out that the algorithm is ill-posed and highly susceptible to noise, as was stated by Kim et al. in a comment in a later paper [18].

Spectral encoding for fs-type THz pulses: spectral envelope information

An extension of the previously-mentioned spectral encoding technique into the high-temporal-resolution domain (no algorithms) does exist [28], and will be discussed now. Although the phase information of the THz pulse is lost, its spectral envelope is retrieved in a single shot with a spectral dynamic range only limited by the inverse Fourier-limited laser pulse length $1/\tau_{\rm FL}$. It is the spectral envelope that provides an indication of the bunch duration, therefore a useful and critical parameter to measure.

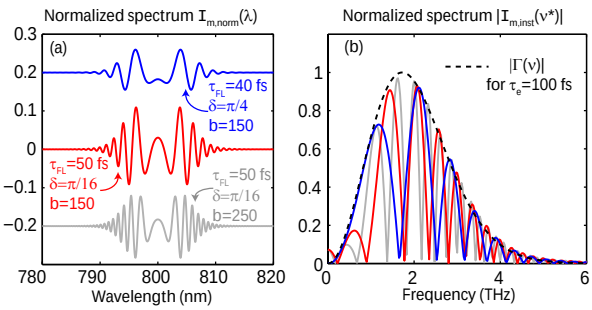

Figure 14: (a) Modeled spectral interferograms $I_{\rm m,norm}(\lambda)$ for various parameters for $\tau_{\rm FL}$, δ, and b. Through the wavelength-to-time parameter substitution $\lambda \rightarrow t^*$ in $I_{\rm m,norm}(\lambda)$ the function $I_{\rm m,inst}(t^*)$ is obtained, with its Fourier transformation $|I_{\rm m,inst}(\nu^*)|$ plotted in (b). The envelopes of the three solid curves in (b) match the original THz spectrum $|\Gamma(\nu)|$ (black dashed curve).

Modeled spectral interferograms are depicted in Fig. 14(a). For these curves the profile $\Gamma(t)$ was modeled based 100 fs (rms) Gaussian electron bunches [for simplification crystal effects are momentarily ignored ($T_{\rm crystal} = 1$)]. The amplitude of $\Gamma(t)$ was set at 0.1 rad. The blue curves in Fig. 14 correspond to various parameters for Fourier limited pulse duration, laser polarization, and the chirp parameter $(\tau_{\rm FL}, \delta, b) = (40\ {\rm fs}, \pi/4, 150)$, the red ones to $(50\ {\rm fs}, \pi/16, 150)$, and the gray ones to $(50\ {\rm fs}, \pi/16, 250)$.

Through Eq. (13) one can convert the wavelength parameter ($\lambda = 2\pi c/\omega_{\rm inst}$) to the time axis t^*. Doing so for $I_{\rm m,norm}(\lambda)$, defined as $[I_M(\lambda) - I_L(\lambda)]/I_L(\lambda)$, the new profile is labeled as $I_{\rm m,inst}(t^*)$. A Fourier transformation of $I_{\rm m,inst}(t^*)$ yields $|I_{\rm m,inst}(\nu^*)|$. The absolute spectra $|I_{\rm m,inst}(\nu^*)|$ for the three curves of Fig. 14(a) are plotted in Fig. 14(b). Also plotted in Fig. 14(b) as the black dashed curve is the THz spectrum $|\Gamma(\nu)|$. One can see that the envelopes of the oscillatory curves $|I_{\rm m,inst}(\nu^*)|$ match the THz spectrum $|\Gamma(\nu)|$. It is because of this matching that

analysis of the spectral interferogram results in single-shot information of the THz spectrum. This new result has been extensively studied and is found to be true for a wide parameter range for b, the amplitude of $\Gamma(t)$, τ_L, $\tau_{\rm FL}$, and τ_e, providing that $\tau_e > \tau_{\rm FL}$ and that $\Gamma(t)$ does not exceed $\simeq 0.3$ rad.

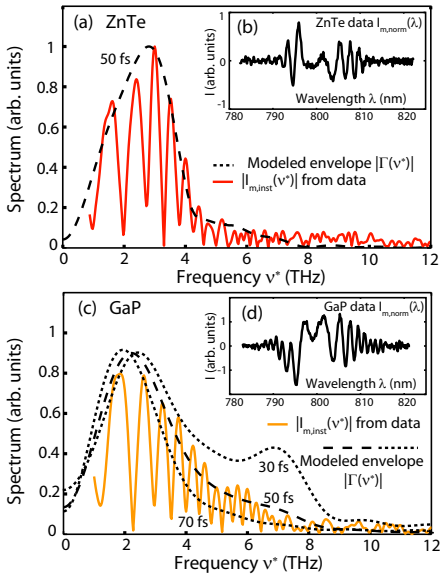

Figure 15: Data from van Tilborg *et al.* [28]. Experimentally obtained modulated laser spectra $I_M(\lambda)$, are normalized [yielding $I_{\rm m,norm}(\lambda)$] and plotted in (b) and (d). After the coordinate substitution $\lambda \rightarrow t^*$ [yielding $I_{\rm m,inst}(t^*)$], the Fourier-transformed curves $|I_{\rm m,inst}(\nu^*)|$ are plotted in (a) and (c). Also displayed in (a) and (c) as the black dashed curves are the THz spectra $|\Gamma(\nu)|$, based on coherent emission from a 50 fs (rms) electron bunch. Modeled curves for a 30 fs and a 70 fs bunch are also shown in (c) to highlight the optimum fit for a 50 fs bunch.

In order to experimentally verify the modeled predictions, we applied the setup to the THz pulses from the LWFA. Each modulated laser spectrum was recorded with a 512x512-pixel 16-bit camera with a resolution of 0.11 nm/pixel. Two typical measured normalized spectral interferograms $I_{\rm m,norm}(\lambda)$ are plotted in Figs. 15(b) and (d), based on a 200-μm-thick ZnTe and GaP EO crystal respectively. The parameters for the probe laser were independently measured with an autocorrelerator and FROG and were found to be $\tau_{\rm FL}$=40 fs (rms) and b=150. After the conversion $I_{\rm norm}(\lambda) \rightarrow I_{\rm inst}(t^*)$, the Fourier-transformed curves $|I_{\rm m,inst}(\nu^*)|$ are displayed in Figs. 15(a) and (c). Also depicted in Figs. 15(a) and (c) as black dashed curves is the spectrum of the THz pulse $|\Gamma(\nu)| = |E_{\rm THz}(\nu)T_{\rm crystal}(\nu)|$. Here the crystal effects [15] were not ignored. Note that the spectral cutoff [as can been seen in the data in Fig. 15(a)] for the ZnTe crystal is ν =4.1 THz. The function $T_{\rm crystal}(\nu)$ for GaP has a cutoff at a higher frequency (ν =8 THz). The black dashed curves in Figs. 15(a) and (c) for $|\Gamma(\nu)|$ are in good agreement with the data [the envelope of $|I_{\rm m,inst}(\nu^*)|$]. The fit was optimized by only varying τ_e to 50 fs (rms).

SUMMARY

In summary, several electro-optic techniques have been presented. In all techniques, the electric field profile of the electron bunch (or the field profile of its coherent emission) is imprinted onto a laser pulse after propagation through an electro-optic crystal. While a scanning technique is most sensitive to weaker THz fields, it intrinsically relies on shot-to-shot reproducibility. Techniques based on non-collinear cross-correlation do provide single-shot information, but the complexity of the systems increases. By analyzing the laser pulse in the frequency domain (through measurement of the laser spectrum) the complexity is reduced. However, the THz pulse information is not directly available, and post-processing of the data is required. Also, either the time resolution, or the phase information is compromised.

Application of EOS to a given accelerator depends on the specific goals and constraint available. Parameters such as the required time resolution, the available laser energy, the demands for online bunch length monitoring, among others, will determine which technique works best.

For now, EOS seems the ideal technique for characterization of sub-picoseconds bunches with single-shot capabilities. Several laboratories worldwide have implemented EOS on their accelerator, and this number will grow as the number of accelerators producing femtosecond bunches steadily increases. Eventually, even the time resolution of EOS (several tens of femtoseconds) will not be sufficient, and a new family of techniques will need to be developed.

This work was supported by the U.S. Department of Energy and the Defense Advanced Research Projects Agency (DARPA).

REFERENCES

[1] P. Catravas, W. P. Leemans, J. S. Wurtele, M. S. Zolotorev, M. Babzien, I. Ben-Zvi, Z. Segalov, X.-J. Wang, and V. Yakimenko, Phys. Rev. Lett. **82**, 5261 (1999).

[2] P. Catravas, E. Esarey, and W. P. Leemans, Phys. of Plasmas **9**, 2428 (2002).

[3] T. Watanabe, J. Sugahara, T. Yoshimatsu, S. Sasaki, Y. Sugiyama, K. Ishi, Y. Shibata, Y. Kondo, K. Yoshii, T. Ueda, and M. Uesaka, Nucl. Instrm. Methods Phys. Res. A **480**, 315 (2002).

[4] C. B. Schroeder, E. Esarey, J. van Tilborg, and W. P. Leemans, Phys. Rev. E **69**, 016501 (2004).

[5] Y. Shibata, T. Takahashi, T. Kanai, K. Ishi, M. Ikezawa, J. Ohkuma, S. Okuda, and T. Okada, Phys. Rev. E **50**, 1479 (1994).

[6] P. Kung, H. Lihn, H. Wiedemann, and D. Bocek, Phys. Rev. Lett. **73**, 967 (1994).

[7] B. Leissner, Ch. Berger, R. Siedling, M. Tonutti, M. Geitz, G. Schmidt, and P. Schmüser, Proceedings of the 1999 Particle Accelerator Conference, IEEE. Part vol. 3, 2172 (1999)

[8] G. Gallot and D. Grischkowsky, J. Opt. Soc. Am. B **16**, 1204 (1999).

[9] S. P. Jamison, A. M. MacLeod, G. Berden, D. A. Jaroszynski, and W. A. Gillespie, Opt. Lett. **31**, 1753 (2006).

[10] D. X. Wang, G. A. Krafft, and C. K. Sinclair, Phys. Rev. E **57**, 2283 (1998).

[11] G. Berden, W. A. Gillespie, S. P. Jamison, E.-A. Knabbe, A. M. MacLeod, A. F. G. van der Meer, P. J. Phillips, H. Schlarb, B. Schmidt, P. Schmüser, and B. Steffen, Phys. Rev. Lett. **99**, 164801 (2007).

[12] S. Banerjee, S. Sepke, R. Shah, A. Valenzuela, A. Maksimchuk, and D. Umstadter, Phys. Rev. Lett. **95**, 035004 (2005).

[13] J. van Tilborg, C. B. Schroeder, Cs. Tóth, C. G. R. Geddes, E. Esarey, and W. P. Leemans, Opt. Lett. **32**, 313 (2007).

[14] Q. Chen, M. Tani, Zhiping Jiang, and X.-C. Zhang, J. Opt. Soc. Am. B **18**, 823 (2001).

[15] J. van Tilborg, C. B. Schroeder, C. V. Filip, Cs. Tóth, C. G. R. Geddes, G. Fubiani, E. Esarey, and W. P. Leemans, Phys. Plasmas **13**, 056704 (2006).

[16] F. L. Pedrotti and L. S. Pedrotti, "Introduction to optics", Prentice Hall International Edition, 1993.

[17] J. van Tilborg, C. B. Schroeder, C. V. Filip, Cs. Tóth, C. G. R. Geddes, G. Fubiani, R. Huber, R. A. Kaindl, E. Esarey, and W. P. Leemans, Phys. Rev. Lett. **96**, 014801 (2006).

[18] K. Y. Kim, B. Yellampalle, A. J. Taylor, G. Rodriguez, and J. H. Glownia, Opt. Lett. **32**, 1968 (2007).

[19] J. Shan, A. S. Weling, E. Knoesel, L. Bartels, M. Bonn, A. Nahata, G. A. Reider, and T. F. Heinz, Opt. Lett. **25**, 426 (2000).

[20] A. L. Cavalieri, D. M. Fritz, S. H. Lee, P. J. Bucksbaum, D. A. Reis *et al.*, Phys. Rev. Lett. **94**, 114801 (2005).

[21] S. P. Jamison, J. Shen, A. M. MacLeod, W. A. Gillespie and D. A. Jaroszynski, Opt. Lett. **28**, 1710 (2003).

[22] G. Berden, S. P. Jamison, A. M. MacLeod, W. A. Gillespie, B. Redlich, and A. F. G. van der Meer, Phys. Rev. Lett. **93**, 114802 (2004).

[23] F. G. Sun, Zhiping Jiang, and X.-C. Zhang, Appl. Phys. Lett. **73**, 2233 (1998).

[24] Zhiping Jiang and X.-C. Zhang, Appl. Phys. Lett. **72**, 1945 (1998).

[25] I. Wilke, A. M. MacLeod, W. A. Gillespie, G. Berden, G. M. H. Knippels, and A. F. G. van der Meer, Phys. Rev. Lett. **88**, 124801 (2002).

[26] B. Yellampalle, K. Y. Kim, G. Rodriguez, J. H. Glownia, and A. J. Taylor, Appl. Phys. Lett. **87**, 211109 (2005).

[27] K. Y. Kim, B. Yellampalle, G. Rodriguez, R. D. Averitt, A. J. Taylor, and J. H. Glownia, Appl. Phys. Lett. **88**, 041123 (2006).

[28] J. van Tilborg, Cs. Tóth, N. H. Matlis, G. R. Plateau, and W. P. Leemans, Opt. Lett. **33**, in press (2008).